Supporting Information for

Accurate estimation of seismic source parameters of induced seismicity by a combined approach of generalized inversion and genetic algorithm: application to The Geysers geothermal area, California

Picozzi M.[1], Oth A.[2], Parolai S.[3], Bindi D.[3], De Landro G.[1], and Amoroso O.[1]

[1]University of Naples Federico II, Italy, [2]European Center for Geodynamics and Seismology, Walferdange, Luxembourg, [3]Helmholtz Centre Potsdam, GFZ German Research Centre for Geosciences, Potsdam, Germany

Contents of this file

Text S1 to S4
Figures S1 to S7

Introduction

This supporting information provides: the text and figures concerning the empirical attenuation and site functions obtained by the GIT; the comparison between the classic and enhanced Genetic Algorithm; finally, a test with synthetic data performed to investigate how the trade-off between the corner frequency and the gamma parameters is mitigated by the enhanced GA inversion approach.

Text S1.

This section presents the empirical attenuation functions obtained by the GIT and the results of the analysis carried out to isolate the contribution due to geometrical spreading from anelastic attenuation. Figure (S1a) shows the empirical attenuation functions plotted with respect to the hypocentral distance up to 20 km for each frequency. All these functions show a rapid monotonic decrease with distance in the first about 10 km, but also different trends with frequency. To isolate the contribution due to geometrical spreading from anelastic attenuation, we fit the empirical attenuation functions with a parametric model of the form:

$$A\left(f, r_{ij}\right) = G(r) \cdot \exp\left[\frac{-\pi f(r - r_0)}{Q(f)v_S}\right], \qquad\qquad [S1]$$

where r_0 the reference distance, $G(r)$ is the geometrical spreading attenuation with respect to r0, Q the apparent quality factor, which we have assumed being frequency-dependent, and v_S the S-wave velocity.

As discussed by Mitchell (2010), the empirical attenuation curves are the result of complex phenomena affecting the seismic waves due to the crust's structure and mechanical properties, while the models used to fit the empirical curves are generally very simple (i.e., as the model in eq. S1). Therefore, the existence of unpredictable effects generates an epistemic source of uncertainty and makes it hard to resolve the inherent trade-off between $G(r)$ and frequency-dependent Q [e.g., Atkinson, 2012; Castro et al., 2013; McNamara et al., 2014].

In this work, we implemented an inversion scheme where both Q and $G(r)$ are frequency-dependent, but this latter, in particular, was modeled with a tri-linear hinged model with crossover distances at 7.5 and 10.5 km (i.e., these latter defined on visual inspection of the empirical curves). Thus, eq. (S1) becomes

$$A(f, r_{ij}) = \begin{cases} \left(\frac{r_0}{r}\right)^{n1} \cdot \exp\left[\frac{-\pi f(r-r_0)}{Q(f)v_S}\right], \text{for } r \leq 7.5 \text{ km} \\ \left(\frac{r_0}{7.5}\right)^{n1} \cdot \left(\frac{7.5}{r}\right)^{n2} \cdot \exp\left[\frac{-\pi f(r-r_0)}{Q(f)v_S}\right], \text{for } 7.5 < r \leq 12.5 \text{ km} \\ \left(\frac{r_0}{7.5}\right)^{n1} \cdot \left(\frac{7.5}{10.5}\right)^{n2} \cdot \left(\frac{10.5}{r}\right)^{n3} \cdot \exp\left[\frac{-\pi f(r-r_0)}{Q(f)v_S}\right], \text{for } r > 12.5 \text{ km} \end{cases} \qquad \text{[S2]}$$

Figure (S1 b) shows three examples of fits between empirical curves and the eq. (S2) model, while Figure (S1 c and d) shows for some representative frequencies the best least-square solution for Q, n1, n2, and n3. We observe that until about 10 Hz the four parameters are confined in a rather narrow range (i.e., average values Q = 170; n1 = 1.12; n2 = 0.95; and n3 = 0.8). For higher frequencies, all the parameters increase, with Q reaching about 1000 and the three geometrical spreading parameters reaching values close to 2. Geometrical spreading faster than r-1 has not uncommonly been found both for empirical data (e.g., Atkinson 2004; Yenier and Atkinson, 2015; Pacor et al., 2016) and numerical simulations for a heterogeneous crust (Frankel, 1991; Chapman and Godbee, 2012). A detailed discussion of the attenuation characteristics in TG areas is not the primary target of this work, and it will be examined in depth in future studies together with results of tomographic analysis.

Text S2.

This section presents the empirical site functions obtained from the non-parametric inversion (Figure S2a). Almost all the stations show amplifications (with respect to station DVB) in the frequency range 5 to about 20 Hz, and for some of them the amplification is very large (e.g., ACR, CLV, DES, DRK, FNF, HVC, MNS, SB4, TCH). These results are in agreement with those obtained by the H/V ratios using directly using the FAS, for which we observed that the H/V ratios of most of the stations (Fig. S2 b) show large amplifications in almost the same frequency range. As discussed and observed by several authors [e.g., Castro et al., 2004; Bindi et al., 2011; Pacor et al., 2016], the vertical component of ground motion may suffer amplification due to the presence in the selected signals of Rayleigh waves generated by complex underground structures. Hence, the H/V ratio technique can fail representing the site response. For this reasons, it is not uncommon like in this study to observe a general common trend but different single features between the GIT and H/V site response estimates.

Text S3.

This section presents the comparison between the classic and enhanced Genetic Algorithm adopted in this study. Sambridge and Mosegaard (2002) classified inversion strategies on the basis of the trade-off between exploration and exploitation criteria. Exploration means trying to minimize the objective function by looking (randomly) in different regions of the parameter space, without considering what has been already learned from previous samples. In contrast, exploitation, which is the ground principle of linearized approaches, means to decide where to sample next by using the previous samples, or the current best fit sample only. Explorative methods (e.g., uniform search, genetic algorithms, simulated annealing, neighbourhood algorithm) are often less efficient in converging toward the global minimum but more robust in avoiding local minima. On the other hand, exploitative algorithms [e.g., steepest descent, Newton-Raphson, amoeba search; see for details e.g, Press et al., 1992; Herrmann, 2002] are generally more efficient in finding a solution, but also more prone to be entrapped in local minima. Hence, their final result could strongly depend on the starting model.

The genetic algorithm applied in this work is the version proposed by Yamanaka and Ishida (1996). The description of the inversion parameters is reported within the main text, while the cost function for the enhanced GA is Eq. [13]. For the classic GA we have the cost function

$$\text{cost}_1 = \sqrt{\sum_{j=1}^{N} \left(\frac{S_o(f) - S(f)}{S_o(f)} \right)^2 / N}, \qquad\qquad \text{[S3]}$$

where the subscript o indicates the observed data and N is the number of data points (i.e., frequencies) in the displacement spectra.

Figure (S3 and S4) shows examples of the inversion results obtained with the two GA approaches for events with magnitude Mw 2 and Mw 3.5. It is worth noting that this analysis has been carried out selecting the same parameter for the random numbers generator. Hence, for each of the two examples (i.e. Mw 2 and Mw 3.5), the first generation of models for both the classic and enhanced GA is the same.

In both cases, more than 30000 models (Figure S3a and S4a, grey lines) have been tested.

Figure (S3a and b) shows the distribution of fc, Mw and γ for the models with misfit within the range of the minimum misfit plus the 10% together with the 16th and 84th percentiles (dashed black lines) and the median value (black line) for the classic and enhanced approaches, respectively. We observe that, the distributions for Mw, fc and γ are narrower in the case of the inversion with the enhanced GA. In both cases, we observe that the minimum misfit as a function of the number of iterations also shows a faster stabilization towards a low stable minimum already after about 50 iterations (Figure S3a and b).

Similar considerations hold also for the comparison between the two GA inversion approaches but considering the event with Mw 3.5 (Figure S4a and b). In this case, however, we observe that the parameter distributions for Mw and fc are slightly different in the two cases, suggesting that while both approaches reached the region with global minimum of the inverse problem, one of the two had a superior capability to explore such area.

To better assess the differences between the two kinds of GA inversion schemes, Figures (S3 c and S4 c) show the percentage decrease of the cost functions with respect to the value at the first iteration as function of the number of generations. In both cases, the cost function $cost_1$ (Eq. S3) shows with respect to $cost_{D(f)}$ (Eq. 13) a reduced capability in finding models with misfit smaller than the one found at the first generations.

All these observations suggest that the new inversion scheme improves the GA capability of converging towards the hyper-volume where the global minimum lies and to better explore its surroundings.

Text S4.

The idea of including the sensitivity as weight within the cost function of the GA inversion is a strategy that we have proposed with the aim to reduce the well-known trade-off between Mo, fc, and gamma. In this section, we focus on the trade-off in the high frequencies between fc and gamma, and we present the result of a test with synthetic data carried out to show how this trade-off between these two parameters is mitigated by the enhanced GA inversion approach. To this purpose, we have considered a synthetic input spectrum obtained considering the following set of parameters: Mw 4, stress drop 3 MPa and gamma equal to 2.5 (i.e., corner frequency equal to 2 Hz; dashed black line in the figure S5 a). Then, a Gaussian random noise has been added to the synthetic input data (red line in the figure S5 a) and the resultant spectrum has been used to study the misfit surface morphology with the variation of fc and gamma, while Mo has been kept fixed. The misfit is computed considering both the cost-functions Eq. S3 (i.e., $cost_1$) and that including the sensitivity (i.e., $cost_{D(f)}$ of equation 13).

Figure S5 b shows the 2D misfit surface and, as expected, indicates the existence of the trade-off between fc and gamma. The trade-off between the parameters can be clearly seen also looking at the 3D view of the misfit surface (Figure S5 c) when the classic misfit function (i.e., $cost_1$) is considered. Indeed, in this case the minimum of the misfit surface corresponding to the true model is not very clear.

On the contrary, Figure S5 c shows that when the cost function including the sensitivity as weight (i.e., $cost_{D(f)}$) is considered, besides a shift towards smaller values of misfit, a very clear and pronounced minimum corresponding to the true model is obtained. This example highlights that the cost function adopted for our analyses (i.e., $cost_{D(f)}$) is less sensitive to the trade-off between fc and gamma and allows the GA to better explore the parameter space around the global minimum.
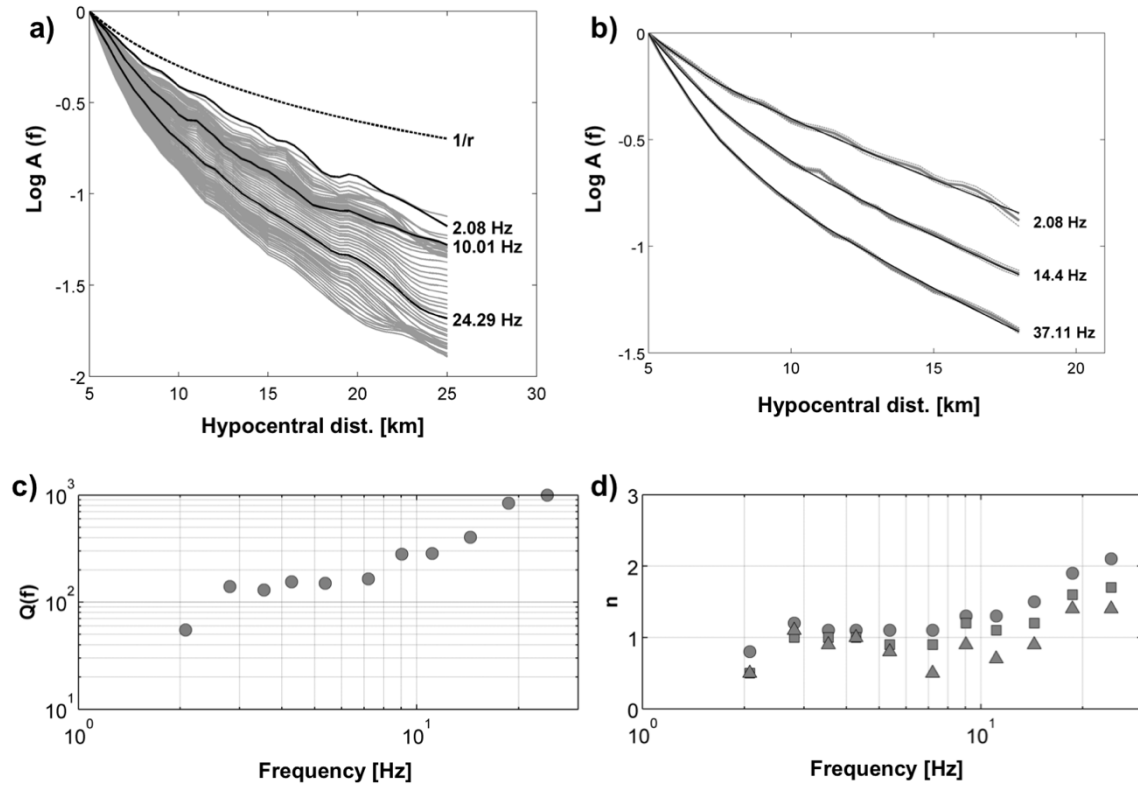
Figures

Figure S1. a) Attenuation-distance curves obtained from the nonparametric inversion (gray lines), and at selected frequencies (black lines); the geometrical spreading, r^{-1} is also plotted (dashed line). b) Comparison between empirical attenuation-distance curves (thick gray lines) +/- 1 standard deviation (thin gray lines) and modeled curves from equation (S2, black lines). c) Quality factor Q versus frequency obtained from equation (S2). d) Geometrical spreading coefficient n obtained from equation (S2) for crossover distances below 7.5 km (dots), between 7.5 and 10.5 km (square), and above 10.5 km (triangles).

Figure S2. a) Site responses derived by the GIT analysis (gray lines), and for the reference station DVB (black line). Amplitude threshold (<2.5) to consider the station site effect free (red line). b) The same as a), but for the Horizontal-to-Vertical spectral ratio of earthquake data (HVE) and computed according to Parolai et al. (2004).
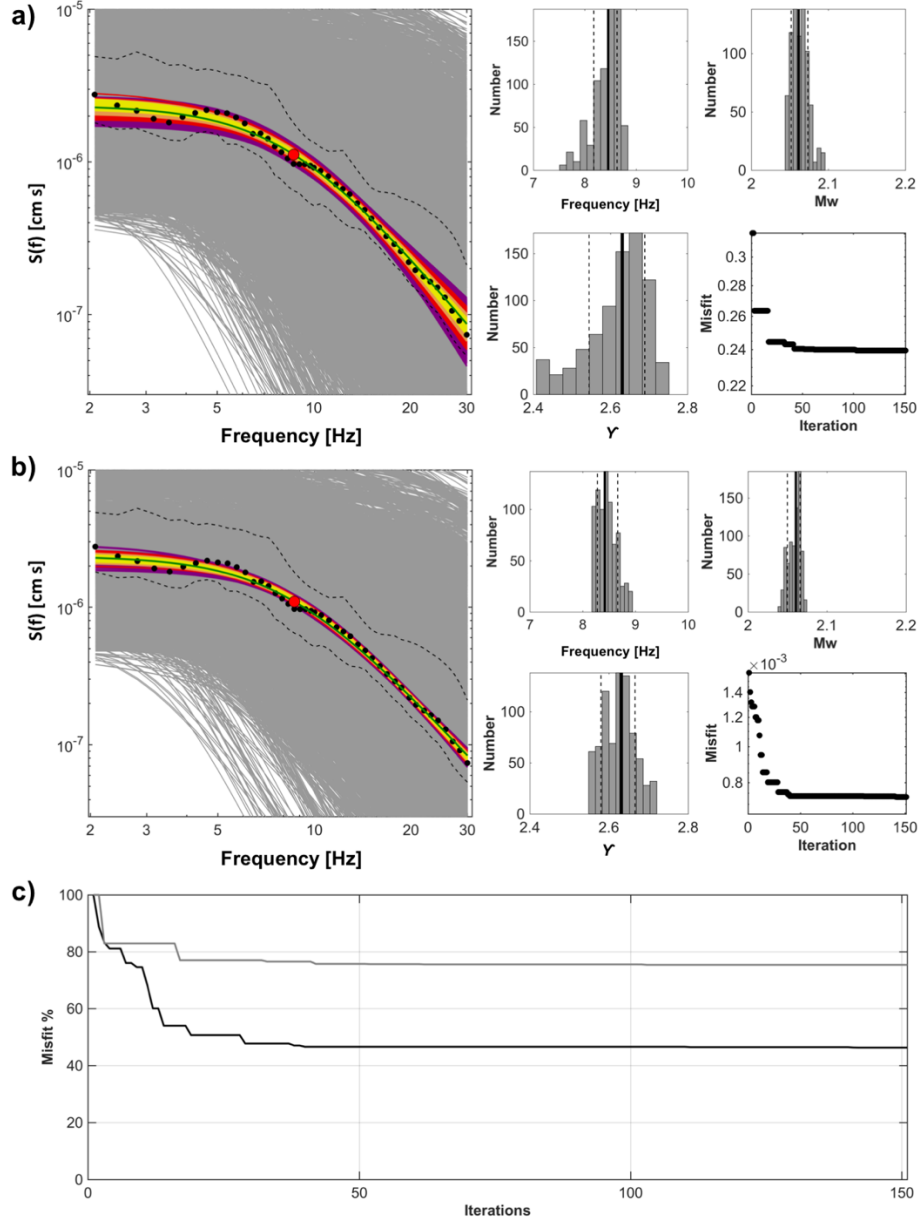
Figure S3. a) Results of the classic GA inversion for an event with Mw 2. Main plot: Experimental source spectra (dots) +/- one standard deviation (dashed lines), tested models (light grey lines), minimum misfit model (green line), models lying inside the minimum misfit plus 10%, 25%, 50% and 100% (i.e., yellow, orange, red and violet lines, respectively), best fit model corner frequency (red dot). Subplots: Distribution of f_c, Mw, and γ for the models with misfit within the range of the minimum misfit plus the 5% (gray bars) together with the 16th and 84th percentiles (dashed black lines) and the median value (black line). Minimum misfit as function of the iteration number (cost function in Eq. S3). b) The same as a), but for the enhanced GA inversion scheme (cost function in Eq. 13). c) Percentage decrease of the cost function in Eq. S3 used by the GA inversion (gray line) and in Eq. 13 used by the enhanced GA inversion (black line) with respect to the value at the first iteration as function of the number of generations.
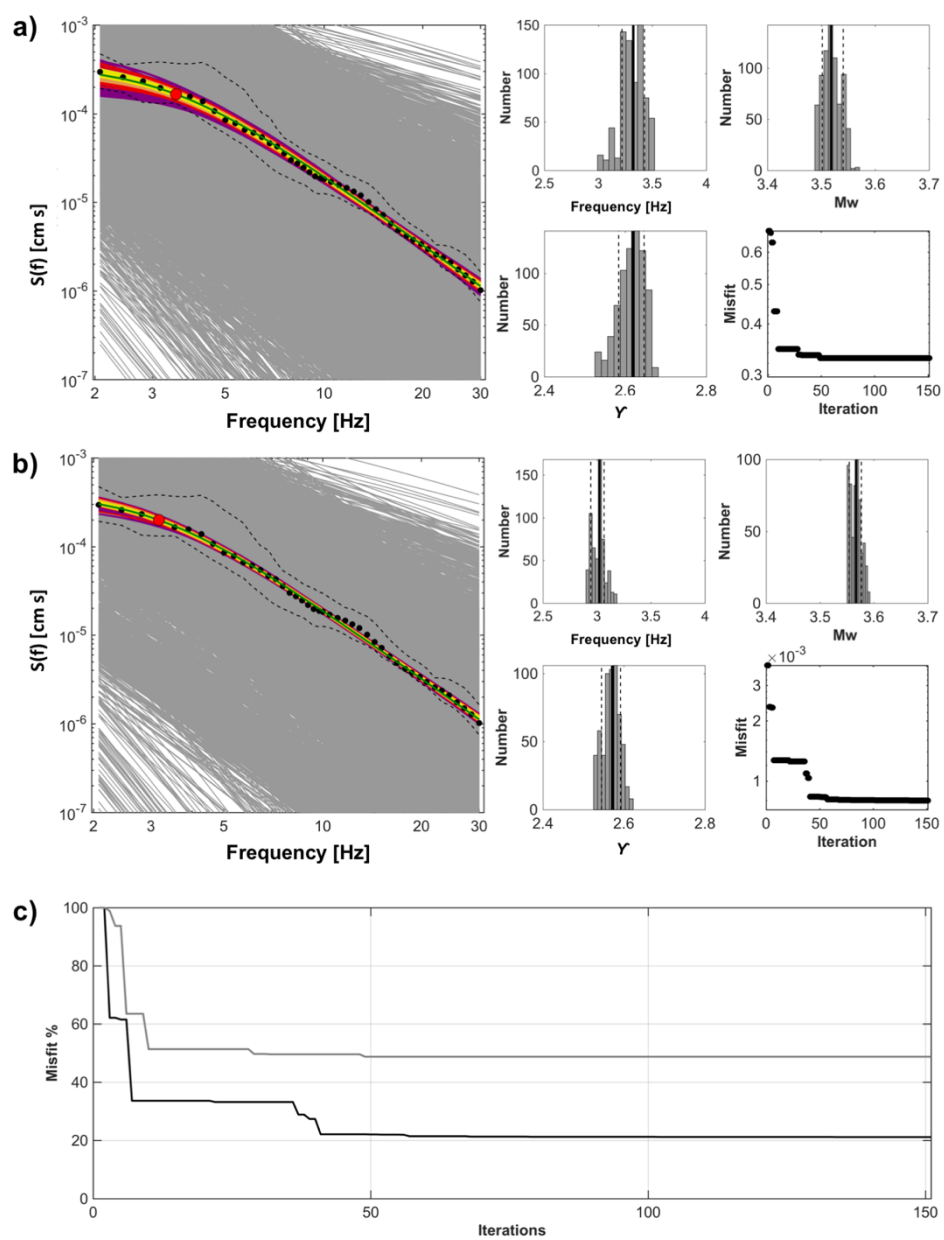
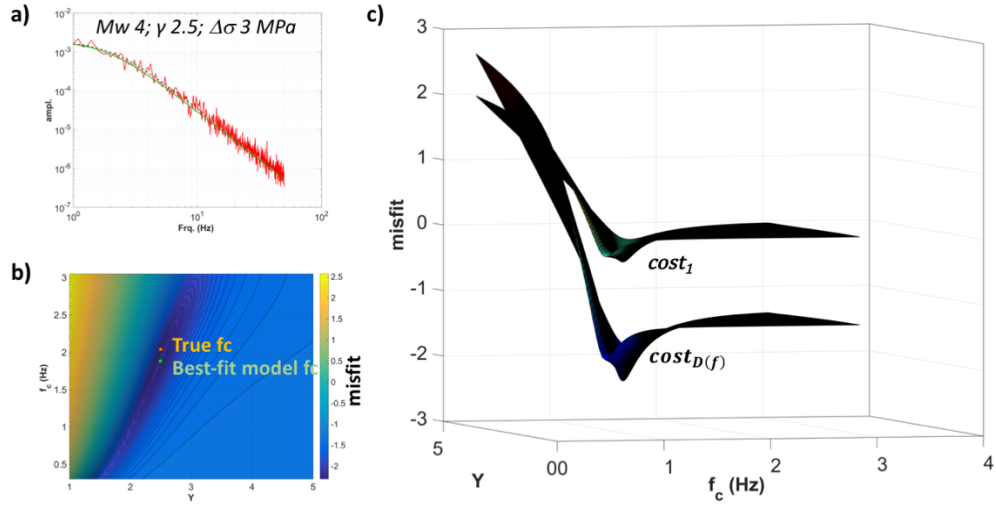**Figure S4.** The same as Figure S3, but for an event with Mw 3.5.

Figure S5. a) Example of synthetic spectra for the set of parameters Mw 4, γ 2.5, and $\Delta\sigma$ 3 MPa (black dashed line), the same with added Gaussian noise (red line) and the one corresponding to the best fit model (green line). b) 2D representation of the $cost_{D(f)}$ function. c) 3D representation of the $cost_1$ and $cost_{D(f)}$ functions.
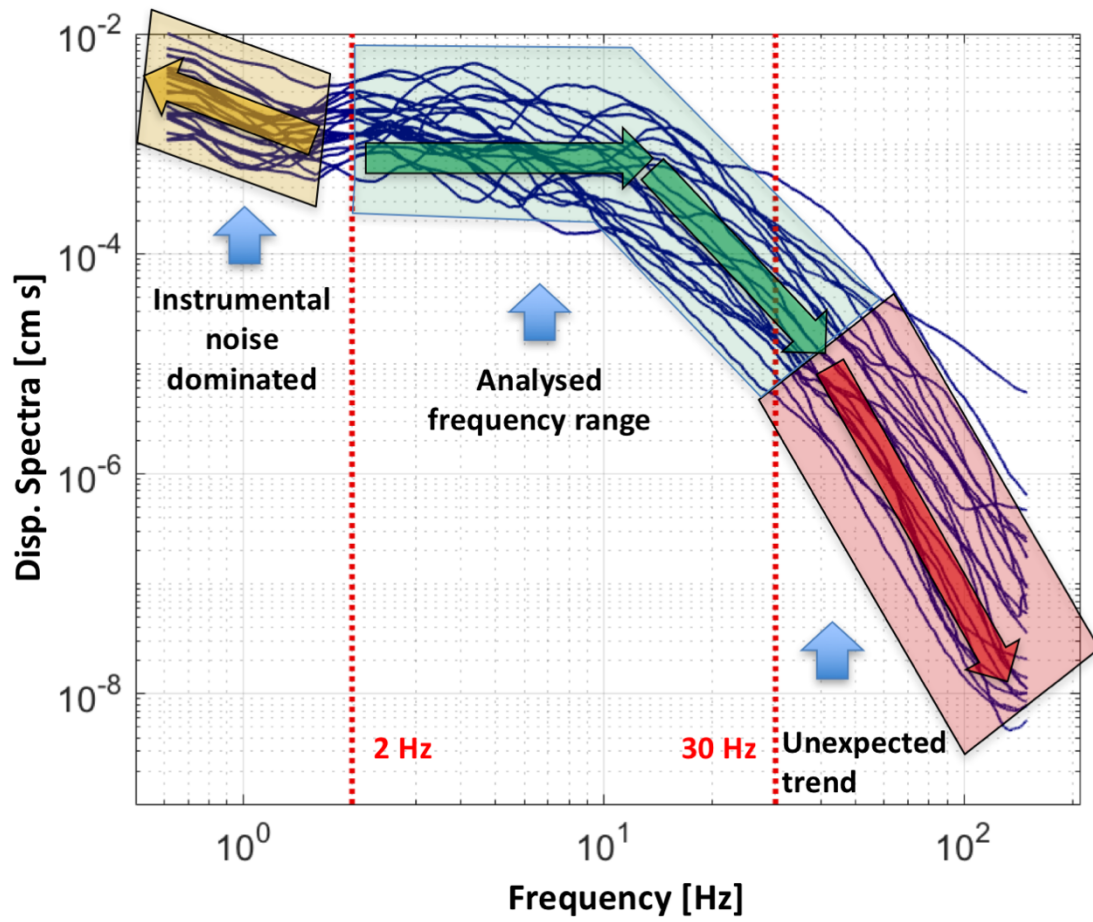
Figure S6. Example of recorded spectra for the same event and uncorrected for the attenuation and site effects (blue lines), lower and upper limits of the frequency band considered for the GA inversion (red dashed lines). Frequencies where the signal is dominated by the instrumental noise are indicated by a light-yellow area, those considered for the GA inversion analysis are indicated by a light-green area, and those discarded because affected by an unexpected trend are indicated by a light-red area.
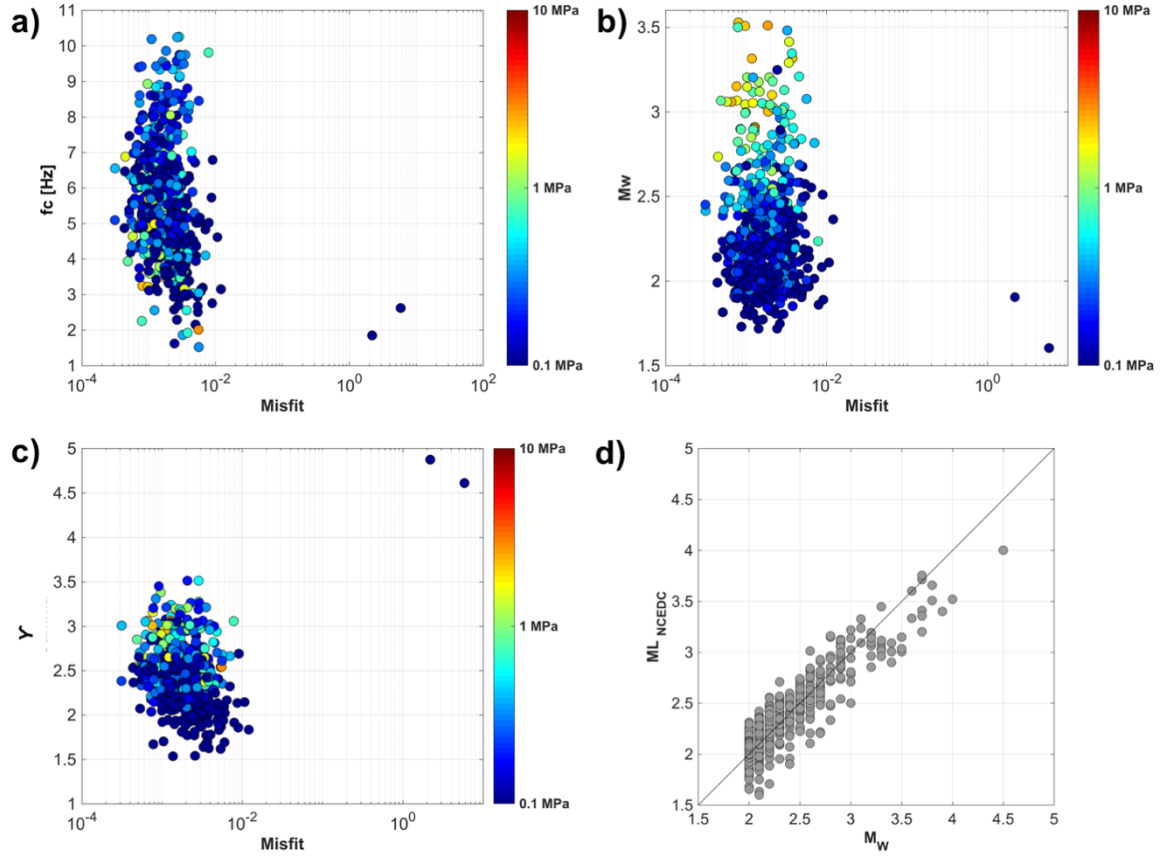
Figure S7. Misfit of 633 best-fit models colored per $\Delta\sigma$ values and plotted with respect to a) the corner frequency, b) the moment magnitude, c) and the parameter γ controlling the high-frequency spectral fall-off. d) Mw versus ML from the NCEDC catalogue.